

Statistical consistency of sign-switching vacuum energy with cosmological observations

Sehjal Khandelwal,^{1,*} Abraão J. S. Capistrano,^{2,†} and Suresh Kumar^{1,‡}

¹*Plaksha University, Mohali, Punjab-140306, India*

²*Universidade Federal do Paraná, Departamento de Engenharia e Exatas,
Rua Pioneiro, 2153, Palotina, 85950-000, Paraná/PR, Brasil
Federal University of Latin American Integration (UNILA),
Applied physics graduation program, Avenida Tarquínio Joslin dos Santos,
1000-Polo Universitário, Foz do Iguaçu, 85867-670, Paraná/PR, Brasil*

We assess dataset agreement and late-time predictive adequacy in Λ CDM and its sign-switching extension, Λ_s CDM, using a suite of Gaussian and exact non-Gaussian consistency diagnostics. Both models are constrained with cosmic microwave background measurements from Planck, ACT, and SPT, baryon acoustic oscillation data from DESI DR2, and low-redshift Type Ia supernova data from PantheonPlus+SH0ES. We find that commonly used Gaussian tension metrics can significantly overstate inconsistencies when broad, non-Gaussian posteriors are combined with tightly constrained datasets. In contrast, the exact non-Gaussian parameter shift indicates excellent consistency between CMB and BAO observations in both models. The Λ_s CDM extension modestly improves geometric compatibility at intermediate redshifts, although reductions in parameter-level tension do not necessarily imply improved predictive consistency. These results highlight the importance of exact, non-Gaussian, and predictive diagnostics for robust assessments of cosmological model consistency.

I. INTRODUCTION

In the past twenty-five years, the amount and precision of cosmological data have increased significantly. The wide range of independent early and late universe probes constrains correlated cosmological parameters with unprecedented accuracy. Multiple independent probes [1], observations of the cosmic microwave background (CMB) anisotropies [2–5], baryon acoustic oscillations (BAO) [6–10], type-Ia supernovae (SNe Ia) [11, 12] and weak gravitational lensing [13–18] collectively establish the spatially flat six parameter Λ CDM model as a remarkable successful baseline description of the universe on large scales and confirmed the accelerated expansion of the universe. The standard Λ CDM model is identified with a cosmological constant, corresponding to a constant equation of state $w = -1$. Despite its remarkable success in describing a wide range of cosmological observations, the physical origin of dark energy remains as one of the most preferred puzzles in modern physics [19–22]. Again, when the predictions of Λ CDM are compared with late-time data, a number of enduring tensions have arisen as the accuracy of cosmological observations has gradually increased over time. One of the most urgent issues in modern cosmology is the difference between early and late universe estimates of the Hubble constant H_0 , which is still statistically significant at the level of $\sim 5-7\sigma$. The measurement of the present-day expansion rate, i.e., the Hubble constant H_0 , is one of the fundamental yet debated aspects of modern cosmology. Discrepancies in the measurements of H_0 from the early universe (e.g., CMB) and late uni-

verse (e.g., SNe Ia, BAO) have led to the Hubble tension [4, 23–30]. This has motivated a rich spectrum of theoretical extensions beyond Λ CDM model, refer to [30–35] and the references therein.

Among these proposals are models in which the vacuum energy density deviates from strictly constant behavior at late times. Sign-switching or transitional vacuum energy scenarios, inspired by the graduated dark energy framework [36] and related phenomenological considerations, enable the effective cosmological constant to grow from a negative value at earlier epochs to a positive value at later eras. Such models like the Λ_s CDM model are one of the concrete realizations of the idea, in which the cosmological constant experiences an abrupt sign change at a characteristic transition redshift z_\dagger . This model has already been proposed and investigated in the literature [37–39], and it has been demonstrated to partially alleviate various late-time anomalies, notably tensions in H_0 and S_8 , while remaining consistent with early-universe observables.

In the present work, we aim to provide a detailed and systematic assessment of the statistical consistency of the Λ_s CDM framework when constrained using current cosmological datasets. As precision improves, it has become increasingly clear that apparent tensions between datasets can depend sensitively on the statistical tools used to quantify them. In particular, Gaussian approximations to posterior distributions can be misleading when posteriors are non-Gaussian, highly correlated, or when one dataset provides substantially weaker constraints than another [40, 41]. In such cases, simple comparisons based on parameter means and covariances may overstate or mischaracterize the degree of inconsistency between datasets.

To address these issues, we adopt a comprehensive suite of dataset-consistency diagnostics discussed in sec-

* sehjal.khandelwal@plaksha.edu.in

† capistrano@ufpr.br

‡ suresh.kumar@plaksha.edu.in

tion V. In addition to standard parameter-shift estimators based on differences in posterior means (DM) and their updated variants (UDM), we consider goodness-of-fit-based statistics such as the difference in maximum a posteriori values (DMAP). We also employ the exact non-Gaussian parameter shift statistic, which is explicitly designed to remain valid in the presence of non-Gaussian posterior shapes. Complementing these parameter space diagnostics, we perform posterior predictive consistency (PPC) tests [42]. Posterior predictive distributions (PPD) have also been used to assess the internal consistency of cosmological probes. For example, the DES Collaboration applied PPD-based tests to evaluate the mutual consistency of different probes in their joint cosmological analysis [43]. This combination of methods allows us to disentangle genuine physical inconsistencies from artifacts arising from posterior geometry or dataset dominance. However, we restrict the PPC analysis to the low-redshift observables (H_0, μ) for clarity and interpretability. The main motivation is the late-time Hubble tension, for which a one-dimensional PPC on H_0 is the most direct predictive test. Furthermore, the low-redshift distance modulus ($\mu(z = 0.01)$) serves as a compact proxy for supernova distance information at the calibration end of the distance ladder, enabling a supplemental distance-based check without the difficulty of fully duplicating supernova datasets [42]. This targeted method allows us to determine whether models calibrated using CMB+LSS data can accommodate both local expansion-rate and nearby-distance limitations.

By applying this multi-pronged statistical analysis to both Λ CDM and its sign-switching extension Λ_s CDM, we hope to clarify to what extent reported tension alleviations in the literature correspond to genuine improvements in predictive adequacy, rather than changes in parameter volume or posterior shape. This work establishes a reliable standard for evaluating late-time extensions of Λ CDM using present cosmological data.

The paper is organized as follows. In Sec. II, we outline the cosmological framework adopted in this work and describe the Λ CDM model together with its sign-switching extension, Λ_s CDM. Sec. III summarizes the observational datasets used, including CMB measurements from Planck, ACT, and SPT, baryon acoustic oscillation constraints from DESI DR2, and low-redshift supernova data from PantheonPlus+SH0ES. In Sec. IV, we detail the statistical methodology and consistency diagnostics employed to quantify the agreement of the dataset. Sec. V presents the results of the tension metrics and posterior predictive consistency tests for both models. Finally, Sec. VI discusses the implications of our findings, and Sec. VII summarizes the main conclusions.

II. COSMOLOGICAL FRAMEWORK AND MODELS

We work within the standard relativistic framework of cosmology, assuming a homogeneous and isotropic universe described by the Friedmann-Lemaître-Robertson-Walker (FLRW) spacetime [19, 44, 45]. The cosmic expansion in the FLRW metric is governed by Einstein's field equations [46], which reduce to the Friedmann equation in a spatially flat universe (with $c = 1$) as

$$H^2 = \frac{8\pi G}{3} \rho_{\text{tot}}, \quad (1)$$

where H is the Hubble expansion rate, ρ_{tot} denotes the total energy density of the cosmic fluid including baryonic matter, cold dark matter, radiation, and a cosmological constant or dark energy, also represented as Λ .

It is convenient to express the expansion rate in terms of redshift as

$$H^2(z) = H_0^2 [\Omega_{r0}(1+z)^4 + \Omega_{m0}(1+z)^3 + \Omega_{de0}f(z)], \quad (2)$$

where Ω_{r0} , Ω_{m0} , and Ω_{de0} denote the present day density parameters of radiation, matter, and dark energy, respectively, and the function $f(z)$ encodes the redshift evolution of the dark-energy component [19, 47]. For a cosmological constant, corresponding to an equation of state, $w = -1$, one has $f(z) = 1(\text{constant})$.

The standard Λ CDM model is obtained by identifying dark energy with a constant Λ and assuming spatial flatness. Despite its minimal assumptions, Λ CDM provides an excellent description of a wide range of cosmological observations as stated in section I. The model is conventionally specified by six parameters describing the physical matter densities, the primordial perturbation spectrum, and the reionization history, and it assumes adiabatic initial conditions and a standard neutrino sector [4].

The other model considered in this work is the Λ_s CDM model. This model is a minimal extension of the standard Λ CDM cosmology, introducing only a single additional parameter, z_\dagger , at which the cosmological constant (Λ) undergoes an abrupt sign switch [48]. All other standard cosmological components, including baryons, cold dark matter, pre-recombination physics, and the inflationary paradigm, remain unaltered. The sign-switching behavior is motivated by recent conjectures such as the graduated dark energy framework [36], which suggests a transition in the nature or behaviour of dark energy across cosmic time. Motivated by recent observational tensions, particularly in measurements of the Hubble constant [49, 50], the model introduces a phenomenological framework where the vacuum energy density is negative in the early universe and becomes positive at $z_\dagger \sim 2$. This transition phenomenologically resembles an AdS-to-dS (Anti-de Sitter to de Sitter) phase shift, a behavior that has been discussed in various theoretical contexts, including effective descriptions motivated

by high-energy frameworks [51]. In its simplest realization, the cosmological constant is modeled as an abrupt sign-switching quantity [37, 38, 52],

$$\Lambda \rightarrow \Lambda_s = \Lambda_{s0} \operatorname{sgn}(z_{\dagger} - z), \quad (3)$$

where $\Lambda_{s0} > 0$ and sgn denotes the signum function, implying that the cosmological constant switches sign across the transition redshift z_{\dagger} . In the present work, we focus explicitly on this abrupt sign-switching realization of the Λ_s CDM model [37–39, 52, 53]. It is important to note, however, that the Λ_s CDM scenario can be readily realized within the Λ CDM framework [54], where the background dynamics are well defined over most redshift ranges, even though an exact description across all redshifts is not possible in the abrupt limit. In this broader context, smooth realizations of the sign transition can be constructed, as discussed for example in [39]. See Refs. [36–39, 53, 55–63] for explicit physical realizations of both abrupt and smooth versions of this framework.

Throughout this work, Λ CDM serves as the reference cosmology against which the statistical and physical performance of Λ_s CDM is evaluated. This enables us to determine if the late-time sign-switching change enhances the internal consistency of cosmological datasets without sacrificing the standard Λ CDM framework’s empirical success.

III. DATASETS

The datasets employed in this analysis are outlined below.

Planck 2018: We use the full Planck 2018 temperature and polarization measurements across both low and high multipoles¹ [64]. The high- ℓ likelihoods include the Planck TT, TE, EE spectra, covering the ranges $30 \leq \ell \leq 2508$ for TT and $30 \leq \ell \leq 1996$ for TE and EE. At large angular scales, we incorporate the low- ℓ temperature likelihood from Commander ($2 \leq \ell \leq 29$) and the low- ℓ polarization likelihood from SimAll ($2 \leq \ell \leq 29$). Additionally, we include the Planck lensing likelihood [65] based on the SMICA reconstruction of the CMB lensing potential. These combined datasets provide a comprehensive set of temperature, polarization, and lensing constraints across the full multipole range probed by Planck [4, 64, 65]. The Planck dataset serves as the primary anchor for our cosmological constraints.

ACT DR6: We use the ACT DR6 ACT-lite likelihood², which provides high-resolution TT, TE, and EE measurements over approximately 40% of the sky and extends the small-scale sensitivity beyond Planck. In our analysis, we adopt the `act_dr6_lenslike`³ configuration with multipole cuts of $\ell_{\max} = 1000$ for TT

and $\ell_{\max} = 600$ for TE and EE. These data improve constraints in the damping-tail regime, complementing Planck’s full-sky coverage with superior small-scale precision. The ACT-lite likelihood focuses on small angular scales, thereby extending the multipole range probed by Planck. The DR6 also includes Plik-lite likelihood cut at $\ell > 1000$ in TT, and $\ell > 600$ in TE and EE [66, 67].

SPT-3G: We use the SPT3G_D1_TnE_lite_candl likelihood⁴ based on temperature and E-mode polarization power spectra from the SPT-3G experiment. The analysis employs the light compressed covariance without CMB lensing, along with internal priors and default data selection. This dataset complements Planck by improving sensitivity to small-scale CMB anisotropies, using publicly available TT, TE, and EE band-power data from ref⁵ [68–70].

This combined compilation of aforementioned CMB datasets is collectively referred to as the **CMB** in forthcoming text. Along with the full CMB dataset, two more datasets are used.

DESI DR2: We use BAO measurements from Dark Energy Spectroscopic Instrument (DESI) Data Release 2 (DR2), including galaxy, quasar, and Lyman- α forest tracers across $0.295 \leq z \leq 2.330$, with distances reported as D_M/r_d , D_H/r_d , and D_V/r_d .

PPS: We use the recently released Pantheon Plus compilation of Type Ia supernovae (SNe Ia). This release allows for the inclusion of low-redshift Cepheid calibration data from the SH0ES collaboration, which plays a key role in the absolute calibration of SNe Ia and is therefore directly relevant to studies of the Hubble tension. For clarity, we refer to this combined dataset as Pantheon Plus + SH0ES (**PPS**). The Pantheon Plus sample contains 1,701 SNe Ia spanning the redshift range $0.0012 < z < 2.26$, as presented in⁶ [23].

IV. METHODOLOGY

We employ multiple consistency diagnostics because Gaussian tension measures can be biased by posterior non-Gaussianity and dataset dominance; the exact non-Gaussian shift and Posterior Predictive consistency (PPC) analysis⁷ [71] provide robust cross-checks that quantify genuine parameter space inconsistency and predictive adequacy, respectively. We restrict the PPC analysis to H_0 and a low-redshift distance-modulus proxy $\mu(z = 0.01)$ because these observables directly probe the late-time expansion history and encapsulate the dominant information relevant to the Hubble tension. Including higher-dimensional or early-universe observables

¹ <https://github.com/benabed/clik>

² <https://github.com/ACTCollaboration/DR6-ACT-lite>

³ https://github.com/ACTCollaboration/act_dr6_lenslike

⁴ https://github.com/SouthPoleTelescope/spt_candl_data/tree/main

⁵ <https://pole.uchicago.edu/public/data/>

⁶ <https://github.com/PantheonPlusSH0ES/DataRelease>

⁷ <https://github.com/sfeeny/hh0>

in the PPC would largely reproduce the constraints already imposed by the CMB likelihoods and would therefore not provide an independent test of late-time predictive adequacy. Now, in order to perform the Markov Chain Monte Carlo (MCMC) analysis for both Λ CDM and Λ_s CDM, we use the CLASS Boltzmann solver [72]. For the standard Λ CDM model, the publicly available CLASS implementation is employed⁸. For the Λ_s CDM scenario, we modify the CLASS background module to implement a non-clustering, sign-switching cosmological constant. In this framework, in addition to the six baseline Λ CDM parameters, we introduce a new parameter z_+ , which denotes the redshift at which the effective cosmological constant changes sign. Specifically, the cosmological constant is negative at early times and positive at late times, corresponding to an AdS-like and a dS-like effective background evolution, respectively. The choice of the cosmological constant in the Λ_s CDM model modifies only the homogeneous background expansion history and assumes that dark energy does not cluster. The step-function behavior serves as a simplifying approximation to a rapid but continuous sign transition. With this modification, the Friedmann equation takes the form

$$\frac{H^2(z)}{H_0^2} = \Omega_{r0}(1+z)^4 + \Omega_{m0}(1+z)^3 + \Omega_{\Lambda_s0} \operatorname{sgn}(z_+ - z), \quad (4)$$

where Ω_{r0} , Ω_{m0} , and Ω_{Λ_s0} denote the present-day density parameters for radiation, matter, and the sign-switching cosmological constant, respectively. All present-day density parameters retain their standard definitions, with the critical density given by $\rho_{c0} = 3H_0^2/(8\pi G)$ and

$$\Omega_{r0} = \frac{\rho_{r0}}{\rho_{c0}}, \quad \Omega_{m0} = \frac{\rho_{m0}}{\rho_{c0}}, \quad \Omega_{\Lambda_s0} = \frac{\rho_{\Lambda_s0}}{\rho_{c0}}. \quad (5)$$

On sub-horizon scales, since dark energy perturbations are neglected, the growth of matter density perturbations remains governed by the standard equation

$$\ddot{\delta} + 2H\dot{\delta} - 4\pi G\rho_m\delta = 0, \quad (6)$$

ensuring that structure formation is affected only indirectly through the modified background expansion [73–75].

The MCMC chains generated using this modified CLASS implementation are subsequently analyzed using the *Tensiometer*⁹ framework to quantify dataset consistency and statistical tensions [76]. The cosmological constraints are obtained by running MCMC simulations using the CLASS Boltzmann solver interfaced with the MontePython framework¹⁰. We explore the full parameter space of both the Λ CDM and Λ_s CDM models using the Metropolis-Hastings sampling algorithm [77]. The

convergence of the chains is verified using the Gelman-Rubin criterion, $R - 1 < 0.01$ [78, 79]. We perform independent MCMC analyses for the three datasets employed in this work: CMB, DESI DR2, and Pantheon-Plus+SH0ES (PPS). The resulting posterior samples are used to compute a range of statistical tension metrics, including the parameter difference (DM), update difference in mean (UDM), maximum a posteriori difference (D_{MAP}), the exact non-Gaussian parameter shift, and the PPC consistency test. The tension metrics are evaluated using the *Tensiometer* package, which operates directly on the MCMC chains. The analysis is performed both on the full shared parameter set to assess the robustness of Gaussian approximations. We additionally evaluate the effective number of constrained parameters and goodness of fit statistics [80] to diagnose posterior non-Gaussianities and dataset dominance effects, ensuring that apparent tensions are not driven by mismatched posterior shapes. We do not perform a separate prior-only MCMC run. All tension metrics are computed directly from the posterior chains obtained from the data analyses, assuming standard, weakly informative priors on the sampled parameters. Since our analysis focuses on posterior-level dataset consistency rather than prior-posterior volume effects, a dedicated prior-only chain is not required. We adopt uniform (flat) priors on the full set of cosmological parameters: the physical baryon density $\omega_b \in [0.018, 0.024]$, the physical cold dark matter density $\omega_c \in [0.10, 0.14]$, the angular size of the sound horizon at recombination parameterized by $100\theta_s \in [1.03, 1.05]$, the logarithmic amplitude of the primordial scalar power spectrum $\ln(10^{10} A_s) \in [3.0, 3.18]$, the scalar spectral index $n_s \in [0.9, 1.1]$, the optical depth to reionization $\tau_{\text{reio}} \in [0.04, 0.125]$, and the additional redshift parameter $z_+ \in [1, 3]$. All prior ranges are chosen to be sufficiently large to ensure that the resulting parameter constraints are dominated by the data rather than by prior-volume effects.

V. STATISTICAL ANALYSIS AND RESULTS FOR VARIOUS TENSION METRICS

In this section, we describe the different tension metrics and present the results of our analysis. The datasets compared are CMB, DESI DR2, and PPS for the two models, Λ CDM and Λ_s CDM. Before presenting the final results and discussion, we first summarize the general behavior and results of all the metrics.

A. Rule Of Thumb

This section describes the different tension metrics as proposed by [40, 81] on the basis of Bayesian inference. The metrics are discussed based on the posterior distributions $P(\theta|D)$ for model M, which is implemented in

⁸ https://github.com/lesgourg/class_public

⁹ <https://github.com/mraveri/tensiometer>

¹⁰ https://github.com/brinckmann/montepython_public

the tensiometer¹¹. All the findings are reported in terms of the effective number of standard deviation N_σ for a two-sided Gaussian probability, described by [81] as

$$P = \text{Erf} \left(\frac{N_\sigma}{2} \right) \quad (7)$$

where P is the likelihood of agreement or disagreement across datasets. Furthermore, $P = 1 - \text{PTE}$ [41] where PTE is the probability to exceed a certain observed value of the estimator Q noted as Q_* for all different metrics, respectively.

In current cosmology, measurements from distinct data sets (for example, CMB vs. large-scale structure PPS) might result in somewhat different values for the same cosmological parameter, such as the Hubble constant. Simple rules of thumb are often used to evaluate these “tensions” before more robust statistical tests are performed [82–84]. The thumb rule given in [85, 86] states that in order to compare two independent measurements of a parameter θ , just calculate the difference in their mean values, normalized by the quadratic sum of their errors. Therefore, the tension metric is given by:

$$T_1 = \frac{|\theta_1 - \theta_2|}{\sqrt{\sigma_1^2 + \sigma_2^2}} \quad (8)$$

A value of T_1 more than 3σ (standard deviations) generally causes alarm and needs additional study into the data, or underlying physics. Another way to determine if two distinct datasets can be defined by the same set of cosmological parameters using their posterior distributions is by determining various tension metrics as discussed in [41, 81]. These essentially compare the odds of two distinct statements: 1) The two datasets D_1 and D_2 are consistent, i.e., they are defined using the same set of parameters. 2) The two datasets D_1 and D_2 are not consistent for the given model, respectively.

B. Posterior Means of Two Datasets in Standard Form

The difference between the posterior means of the two datasets $D_1(\theta)$ and $D_2(\theta)$ for the inferred parameters is determined using the quadratic form defined as [41, 81]

$$Q_{\text{DM}} = (\hat{\theta}_{D_1} - \hat{\theta}_{D_2})^T C^{-1} (\hat{\theta}_{D_1} - \hat{\theta}_{D_2}) \quad (9)$$

where $C = \hat{C}_{D_1} + \hat{C}_{D_2}$ is the covariance matrix of $(\hat{\theta}_{D_1} - \hat{\theta}_{D_2})$. $\hat{\theta}_i$ and \hat{C}_i are the mean and covariance matrix on the parameter space for datasets D_1 and D_2 . With the Gaussian choice of posterior distribution, the quadratic form of Q_{DM} follows a χ^2 distribution with

$\nu = \text{rank}[\hat{C}_{D_1} + \hat{C}_{D_2}]$ degrees of freedom (dof) [81] respectively.

According to Table I, the Λ CDM shows a weak to moderate tension between DESI DR2 and CMB, consistent with the moderate mean differences seen in Fig. 1(a). From Table II, the strongest tension arises between the joint CMB+DESI DR2 dataset and PPS, which means the two datasets assume two different parameter values in this model.

In the Λ_s CDM model, DESI DR2 and CMB represent the lowest tension among all analyses (Table III and Fig. 2(a)). The comparison between CMB+DESI DR2 and PPS yields an extremely large tension of 7.7σ , driven primarily by the Gaussian approximation assumed in the DM metric. We point out that although the Gelman–Rubin criterion $R - 1 \ll 0.01$ is satisfied, we reinforce that R is a necessary but not sufficient condition for full exploration, particularly for extended cosmological models where posteriors can be highly non-Gaussian and exhibit long degeneracy directions. In such cases, multiple Metropolis–Hastings chains may show small between-chain variance (hence $R \sim 1$) while still mixing slowly along weakly constrained directions, leading to residual Monte Carlo noise visible in marginal/triangle plots. This behavior is consistent with the observation that DESI DR2 in Λ_s CDM is comparatively less convergent and that DR2 alone does not fully converge when used independently. To ensure robustness of our results, we additionally verified stability of the constraints with adequate effective sample sizes (ESS) for the parameters. The bulk ESS is $\sim 6 \times 10^2 - 8 \times 10^2$ and tail ESS is $\sim 1.1 \times 10^3 - 1.4 \times 10^3$, indicating that medians and 68% C.I. are stable to Monte Carlo error. The largest rank-split R we find is ~ 1.014 for ω_{cdm} , consistent with mild residual slow mixing but not affecting our results.

It is important to note that DM accounts for parameter correlations, while the rule of thumb does not, leading to different tension estimates [81].

TABLE I. Parameter Shift Consistency Results for Λ CDM Model Using CMB+DESI DR2 Dataset Combination in full shared parameter set. In the table below UDM₁ refer to UDM_(CMB→DESIDR2) and UDM₂ refer to UDM_(DESIDR2→CMB), respectively. P is truncated to two decimals in the Tables; PTE and N_σ are the authoritative values.

Metric	ν	Q_*	P	PTE	N_σ
DM	4	11.2	0.98	0.022	2.25
UDM ₁	2	4.5	0.9	0.1	1.6
UDM ₂	3	21.9	0.99	6.7×10^{-5}	3.98
DMAP	4	6.4	0.83	0.17	1.4
Exact Param. Shift	–	–	0.97	0.026	2.2
Rule of Thumb:	$N_{\Omega_b} = 0.0914$	$N_{\Omega_m} = 2.00$			
	$N_{H_0} = 2.495$	$N_{r_d} = 0.5931$			

¹¹ <https://github.com/mraveri/tensiometer>

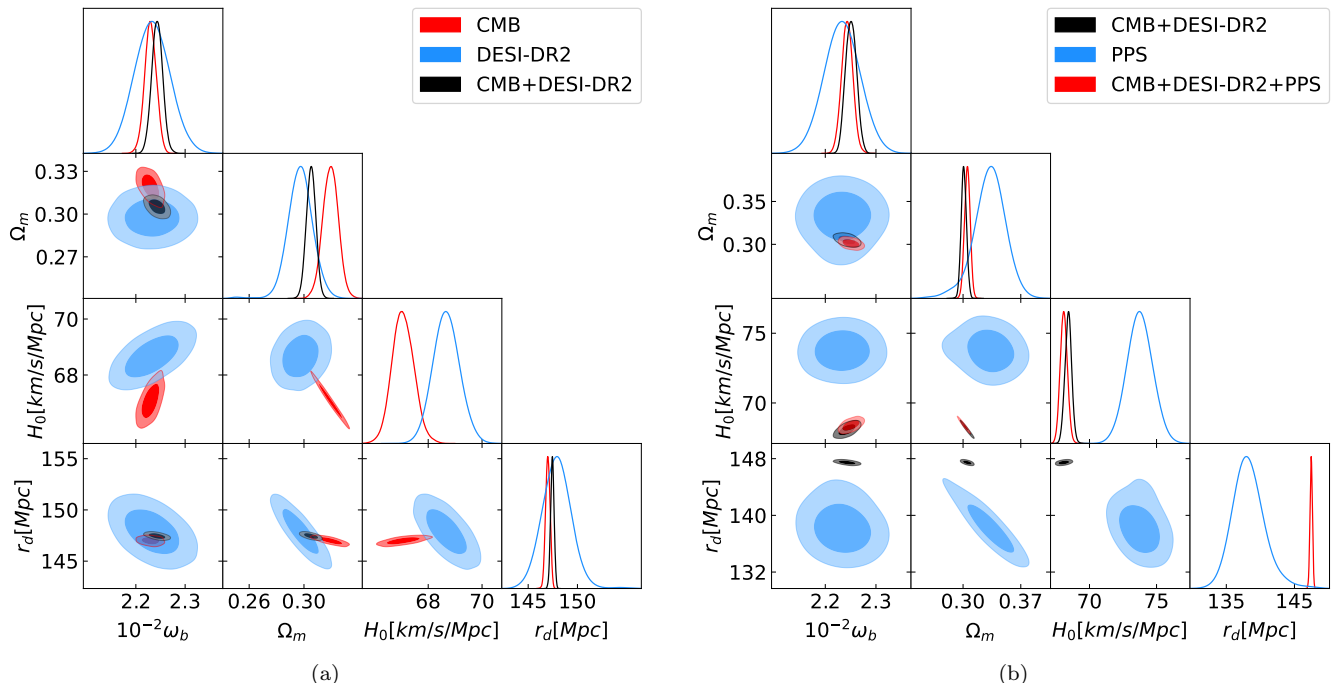


FIG. 1. Triangular plots for the Λ CDM model. (Left) Comparison between CMB (red), DESI DR2 (blue), and their combination (black). (Right) Comparison between the combined CMB+DESI DR2 dataset (black), PPS (blue), and the full combination (red). Diagonal panels show 1D posteriors; off-diagonal panels show 68% and 95% contours.

TABLE II. Parameter Shift Consistency Results for Λ CDM Model Using DESI DR2+CMB+PPS Dataset Combination in full shared parameter set. In the table below UDM_1 refer to $UDM_{(CMB+DESIDR2 \rightarrow PPS)}$ and UDM_2 refer to $UDM_{(PPS \rightarrow CMB+DESIDR2)}$ respectively. P is truncated to two decimals in the Tables; PTE and N_σ are the authoritative values.

Metric	ν	Q^*	P	PTE	N_σ
DM	4	39.8	1	4.6×10^{-8}	5.5
UDM_1	2	1.2	0.45	0.6	0.58
UDM_2	2	11.35	0.99	3.4×10^{-3}	2.92
DMAP	4	20	0.99	0.0005	3.5
Exact Param. Shift	-	-	$< 2 \times 10^{-7}$	0.999	≥ 5.1
Rule of Thumb:	$N_{\Omega_b} = 0.2678$	$N_{\Omega_m} = 1.33$			
	$N_{H_0} = 5.6784$	$N_{r_d} = 3.7417$			

C. Posterior Means of Two Datasets in Updated Form

This quantity is referred to as the updated difference in mean since it quantifies the differences in parameters of one dataset D_1 and the joint dataset D_{12} referred to as the UDM metric [41]. The updated difference in the mean quadratic form is:

$$Q_{UDM} = (\hat{\theta}_{D_1} - \hat{\theta}_{D_{12}})^T C^{-1} (\hat{\theta}_{D_1} - \hat{\theta}_{D_{12}}) \quad (10)$$

where $C = \hat{C}_{D_1} - \hat{C}_{D_{12}}$ is the covariance matrix of $(\hat{\theta}_{D_1} - \hat{\theta}_{D_{12}})$. $\hat{\theta}_{D_{12}}$ and $\hat{C}_{D_{12}}$ are the mean and covari-

TABLE III. Parameter Shift Consistency Results for Λ_s CDM Model Using CMB+DESI DR2 Dataset Combination in full shared parameter set. In the table below UDM_1 refer to $UDM_{(CMB \rightarrow DESIDR2)}$ and UDM_2 refer to $UDM_{(DESIDR2 \rightarrow CMB)}$ respectively. P is truncated to two decimals in the Tables; PTE and N_σ are the authoritative values.

Metric	ν	Q^*	P	PTE	N_σ
DM	6	1.6	0.05	0.95	0.061
UDM_1	3	0.95	0.185	0.81	0.23
UDM_2	4	0.33	0.0125	0.99	0.016
DMAP	6	2.98	0.19	0.81	0.24
Exact Param. Shift	-	-	0.66	0.34	0.95
Rule of Thumb:	$N_{\Omega_b} = 0.0328$	$N_{\Omega_m} = 0.50$			
	$N_{H_0} = 0.70$	$N_{r_d} = 0.133$			
	$N_{P1} = 0.75$	$N_{\Omega_{cdm}} = 0.098$			

ance matrix obtained from the statistical analysis with the joint dataset D_{12} .

All these quadratic forms are central and can be degenerate, depending on the covariance rank. For Gaussian posteriors of both the datasets D_1 and D_{12} , Q_{UDM} follows a chi squared distribution with rank $\nu = \text{rank}[\hat{C}_{D_1} - \hat{C}_{D_{12}}]$ dof. The UDM statistic is directional in principle as it measures how much the updated dataset shifts the posterior mean of the base dataset, and this depends on which dataset plays each role [87]. It has applications in non-Gaussian metrics.

In the Λ CDM model, updating CMB with DESI DR2

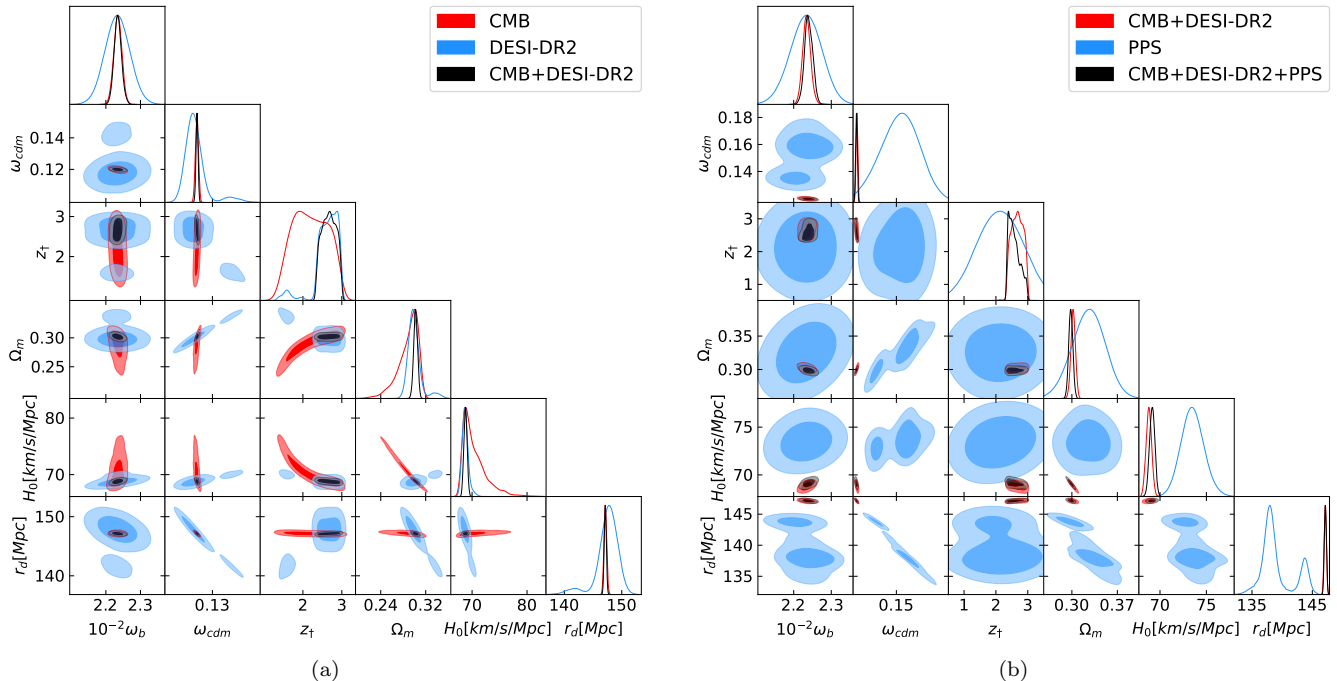


FIG. 2. Triangular plots for the Λ_s CDM model. (Left) Comparison between CMB (red), DESI DR2 (blue), and their combination (black). (Right) Comparison between CMB+DESI DR2 (red), PPS (blue), and the full combination (black). Diagonal panels show 1D posteriors; off-diagonal panels show 68% and 95% credible regions.

TABLE IV. Parameter Shift Consistency Results for Λ_s CDM Model Using DESI DR2+CMB+PPS Dataset Combination in full shared parameter set). In the table below UDM_1 refer to $UDM_{(CMB+DESIDR2 \rightarrow PPS)}$ and UDM_2 refer to $UDM_{(PPS \rightarrow CMB+DESIDR2)}$ respectively. P is truncated to two decimals in the Tables; PTE and N_σ are the authoritative values.

Metric	ν	Q^*	P	PTE	N_σ
DM	6	77.4	1	1.24×10^{-14}	7.7
UDM_1	3	0.6	0.103	0.9	0.13
UDM_2	3	67.59	1	1.40×10^{-14}	7.6
DMAP	6	15.7	0.98	0.015	2.42
Exact Param. Shift	-	-	$< 2 \times 10^{-7}$	0.999	≥ 5.1
Rule of Thumb:	$N_{\Omega_b} = 0.0378$	$N_{\Omega_m} = 1.1430$			
	$N_{H_0} = 3.9508$	$N_{r_d} = 2.8155$			
	$N_{P1} = 0.9159$	$N_{\Omega_{cdm}} = 2.7893$			

yields a weak tension of 1.6σ indicates a smaller shift, whereas when DESI DR2 is updated with CMB, the obtained tension increases to 3.98σ implies that the CMB dataset is more consistent internally. According to Eq. 10, the tension is higher if the mean shift is higher or $|\hat{C}_{D_1} - \hat{C}_{D_{12}}|$ is small. Here, the covariance matrix is quite small, and the posterior mean is non-negligible, making the Q^* estimator (or Q_{UDM} estimator) and corresponding N_σ higher. Furthermore, UDM_2 in Table I has 3 effective degrees of freedom. Since DESI DR2 alone is relatively weak, CMB data add a lot of information and significantly tighten three independent combinations of param-

eters. A similar behavior appears with the PPS dataset. Updating CMB+DESI DR2 with PPS gives a negligible tension of 0.58σ , while updating PPS with the combined data increases the tension to 2.92σ . This asymmetric tension arises because PPS has an extremely large posterior; it covers almost the entire region of the combined dataset's posterior, and the update dataset (CMB+DESI DR2) forces PPS into a much narrower parameter region.

In the Λ_s CDM model, we first consider the case of CMB+DESI DR2. Updating CMB with DESI DR2 yields a tension of 0.23σ , while updating DESI DR2 with CMB gives 0.016σ , thus it substantially decreases. Both tensions are negligible, consistent with Fig. 2(a), where the contours overlap closely, with DESI DR2 appearing less convergent. Next, we analyze the CMB+DESI DR2 and PPS comparison. Updating CMB+DESI DR2 with PPS gives a tension of 0.13σ , whereas updating PPS with the combined dataset results in an extremely strong tension of 7.6σ , which means the posterior mean is dragged a long distance, far beyond what PPS would “expect” statistically, inducing tension in between the datasets. In this case, the difference between the means of the two distributions becomes significant.

D. Goodness-of-fit type test

Using this metric, we evaluate the difference of log-likelihoods at the Maximum A Posteriori (MAP) point

for two datasets considered jointly and separately in statistical analysis using the estimator defined in [41, 81]

$$Q_{\text{DMAP}} = -2 \ln \mathcal{L}_{12}(\theta_p^{12}) + 2 \ln \mathcal{L}_1(\theta_p^1) + 2 \ln \mathcal{L}_2(\theta_p^2) \quad (11)$$

θ_p^i denotes the MAP parameters for dataset $i = (1, 2, 12)$. This statistic quantifies the loss in goodness of fit when two independent datasets are combined [81]. The normalization factors of the likelihoods cancel for the independent datasets, ensuring that Q_{DMAP} depends only on the shape of the likelihood surfaces and not on their absolute normalization. Therefore, the resulting value of Q_{DMAP} measures how much statistical tension exists between the two datasets. Under the assumption of Gaussian priors, the distribution of Q_{DMAP} can be approximated as $Q_{\text{DMAP}} \sim \chi^2(N_{\text{eff}}^{(1)} + N_{\text{eff}}^{(2)} - N_{\text{eff}}^{(12)})$, where the sum of N_{eff} is the number of dof [81], and the effective number of constrained parameters for each dataset is defined as

$$N_{\text{eff}}^{(i)} = N - \text{tr} \left[C_{\Pi,i}^{-1} C_{p,i} \right] \quad (12)$$

where N is the number of sampled parameters. $C_{\Pi,i}$ and $C_{p,i}$ are the covariance matrices of the posterior and prior distributions for the i -datasets, respectively [40, 41, 76, 81, 85, 87, 88]. Therefore, Q_{DMAP} serves as a useful tool to measure how well the data fit the theoretical predictions, though it does not provide a direct estimate of the inconsistency between individual parameters. DMAP cannot be compared to DM because, unlike DM, DMAP does not take the covariance matrix into account.

In the Λ CDM model, for the joint CMB+DESI DR2 dataset, DMAP gives 1.4σ tension, while DESI DR2+CMB+PPS gives 3.4σ tension, indicating that the broad posterior of PPS pulls the best-fit value away from the CMB+DESI DR2 solution. The results are in agreement with Fig. 1(a) and Fig. 1(b). Since flat uninformative priors are used, the effective degrees of freedom reported in Tables I-IV correspond to the numerical rank of the parameter-difference covariance matrix and therefore may be smaller than the total number of sampled parameters. We also point out that with bounded priors, N_{eff} depends on how much the posterior shrinks relative to those bounds; thus, it will not be equal to the dimension.

In the Λ_s CDM model, in Fig. 2(a), we can see that the maximum of the joint posterior is located in the 1σ contour of the corresponding posteriors obtained considering only one dataset. Similarly, in Fig. 2(b), we can see that the maximum of the joint posterior is located in the 1σ contour of CMB+DESI DR2 posterior, except for the H_0 and r_d value which, lies in the 2σ contour. Thus, this gives rise to a mild tension as quantified in Table IV. Both the observations are in agreement with the results quantified in Tables III and IV. Note that the tensions obtained in all the above cases, for both models, remain lower than the H_0 tension estimated by the rule of thumb. This indicates that the overall tension

decreases when the full shared parameter space is taken into account.

It is important to point out that in our analysis, we adopt weakly informative uniform priors over ranges that are substantially broader than the final posterior support. Because the posterior distributions are strongly data-dominated within these bounds, prior-volume effects are subdominant for the primary tension estimators. That said, we emphasize that N_{eff} should not be interpreted as the literal dimensionality of the parameter space, but as a measure of posterior contraction relative to the adopted prior domain. Moreover, due to the fact that the priors are chosen to be sufficiently broad and encompass regions far beyond the posterior bulk, the resulting N_{eff} values primarily reflect data-driven constraints. Thus, while prior-only chains could in principle refine the interpretation of N_{eff} , their omission does not affect the parameter-shift or posterior predictive conclusions presented here. The core tension diagnostics are computed directly from posterior samples and remain robust under variations of prior width within reasonable bounds.

E. Exact Parameter Shift in Non-Gaussian Metrics

To robustly quantify dataset consistency, we employ the non-Gaussian exact parameter shift statistic introduced in [81] and further used in [40]. This method evaluates the parameter difference probability density $P(\Delta\theta)$, where $\Delta\theta = \theta_1 - \theta_2$ is the difference between the means of the posterior parameters that correspond to datasets 1/2. The general expression for two uncorrelated datasets is given by [41]

$$P(\Delta\theta) = \int P_A(\theta) P_B(\theta - \Delta\theta) d\theta, \quad (13)$$

The probability to identify tension or statistical significance of the shift is calculated corresponding to the probability that the parameter shift exceeds zero $\Delta\theta = 0$. Therefore, $\Delta = \int_{P(\Delta\theta) > P(0)} P(\Delta\theta) d\Delta\theta$. Here, the assigned probability to identify the tension is $P = \Delta$ [41] and the equivalent N_σ is calculated by inverting Eq. 7. Unlike Gaussian tension metrics, which rely on linear approximations and can be highly biased by skewed, non-Gaussian exact parameter shift metric incorporates the full parameter space structure and asymmetric support to produce a conservative and model-independent measurement of tension. In practice, the probability Δ is estimated numerically from Monte Carlo samples of the shift distribution. Since the estimator is based on a finite number of samples, cases in which no samples fall below the no-shift density correspond to an upper bound on Δ rather than a vanishing probability. In such cases, we report conservative bounds using a count-based estimator, $\Delta \sim (k + 1)/(n + 1)$, where k is the number of samples with density lower than $P(0)$ out of n total test samples. This procedure avoids numerical artifacts and

ensures a well-defined finite-sample interpretation of the shift significance.

In Tables I and III, it is clearly seen that for the CMB and DESI DR2, the values of the non-Gaussian exact parameter shift and that of Q^* for DM metric is almost similar, indicating very small tension between the dataset combinations. Also, the lower values of DM in Λ_s CDM indicate that the model agrees more between shared space datasets. Again, in Tables II and IV, in earlier Gaussian and update-based metrics, the apparent tensions involving PPS appear exaggerated due to extreme posterior broadness and covariance compression. However, when applying the exact non-Gaussian parameter shift with finite-sample control, we find that the no-shift point lies in a very low-density region of the shift distribution. Using batched Monte Carlo estimation totaling 5×10^6 test samples, we find zero samples with density lower than the no-shift point, implying a conservative bound $p_{shift} < 2 \times 10^{-7}$, corresponding to $\sigma_{shift} \geq 5.1$. As a result, this indicates that the posteriors occupy disjoint regions of parameter space once their full non-Gaussian structure is accounted for. As an independent Gaussian cross-check, we also compute the Mahalanobis distance [89–91] d_M of the shift distribution and obtain $d_M \sim 5.12$, consistent with a substantial joint displacement in the correlated parameter space. Also, this bound is stable under variations of the KDE bandwidth by a factor of four 0.5 – 2.0, indicating that our result is not driven by smoothing choices or numerical artifacts.

To clarify the relationship between Gaussian and exact non-Gaussian tension estimators, we emphasize that agreement or disagreement between these metrics depends sensitively on the geometry of the posterior distributions in the shared parameter space. Gaussian estimators such as DM and UDM approximate the shift between datasets using only the first two moments of the posterior, implicitly assuming local quadratic behavior of the log-likelihood around the posterior mean. This approximation can misrepresent tension when posterior distributions are highly skewed, non-elliptical, truncated by priors, or dominated by one dataset.

For the CMB+DESI DR2 comparison, both Gaussian and exact non-Gaussian parameter-shift statistics yield consistent results, indicating substantial posterior overlap. This agreement arises because both posteriors are compact and approximately elliptical in the shared parameter subspace, such that the quadratic approximation remains valid. On the other hand, when comparing CMB+DESI DR2 with PPS, Gaussian estimators yield large apparent tensions, and the exact non-Gaussian shift confirms that the no-shift point lies in a region of extremely low probability density. The agreement between Gaussian and exact estimators in this case does not contradict our earlier caution regarding Gaussian metrics. That said, it reflects the fact that the dominant effect is not posterior skewness alone, but a genuine displacement of high-probability support in correlated parameter

directions.

F. Posterior Predictive Consistency Tests

The posterior predictive distribution describes the probability distribution of future or replicated data conditioned on the observed data through the posterior over model parameters [43, 92, 93]. Formally, it is defined as

$$p(y^{\text{rep}} | y) = \int p(y^{\text{rep}} | \theta) p(\theta | y) d\theta, \quad (14)$$

where y^{rep} denotes data that could be generated under the model, y represents the observed data, and θ is the set of model parameters [92, 93]. The integrand consists of the sampling distribution for the replicated data conditioned on the parameters and the posterior distribution of the parameters given the observed data. This construction provides a way to assess model adequacy: if a model offers a good description of the observed data, then replicated data drawn from the posterior predictive distribution should resemble the observations. Consequently, model checking can be performed by generating replicated data sets and comparing them to the observed data using suitable discrepancy measures. To quantify this comparison, one may define a test statistic $T(y)$ that captures a relevant feature of the data, and evaluate the same statistic $T(y^{\text{rep}})$ on the replicated data. A Bayesian posterior predictive p -value is then given by

$$p_{\text{ppc}} = \Pr[T(y^{\text{rep}}) \geq T(y) | y], \quad (15)$$

which represents the probability that the test statistic computed from replicated data exceeds that obtained from the observed data [42, 94, 95]. Values of p_{ppc} close to zero or unity indicate a potential mismatch between the model and the observed data, while values near the middle of the unit interval suggest adequate model consistency.

In this work, PPC tests are performed for both the Λ CDM and Λ_s CDM models using posterior samples obtained from CMB and DESI DR2 and large-scale structure data. From each posterior draw, replicated observables are generated for the Hubble constant H_0 and a low-redshift supernova distance modulus $\mu(z)$ evaluated at $z = 0.01$. To quantify discrepancies, we consider multiple statistics: a one-dimensional statistic for H_0 , a corresponding statistic for μ , a joint χ^2 statistic constructed from (H_0, μ) , and a maximum joint discrepancy statistic designed to capture worst-case deviations. Posterior predictive p -values are computed as the fraction of replicated discrepancies exceeding the observed value, with Monte Carlo uncertainties estimated from repeated draws.

For the Λ CDM model, the PPC analysis reveals a severe inconsistency with the local measurement of the Hubble constant. The posterior predictive distribution yields a Planck-like expansion rate, and the observed value $H_0 = 73.04 \pm 1.04 \text{ km s}^{-1} \text{ Mpc}^{-1}$ [96] lies deep in

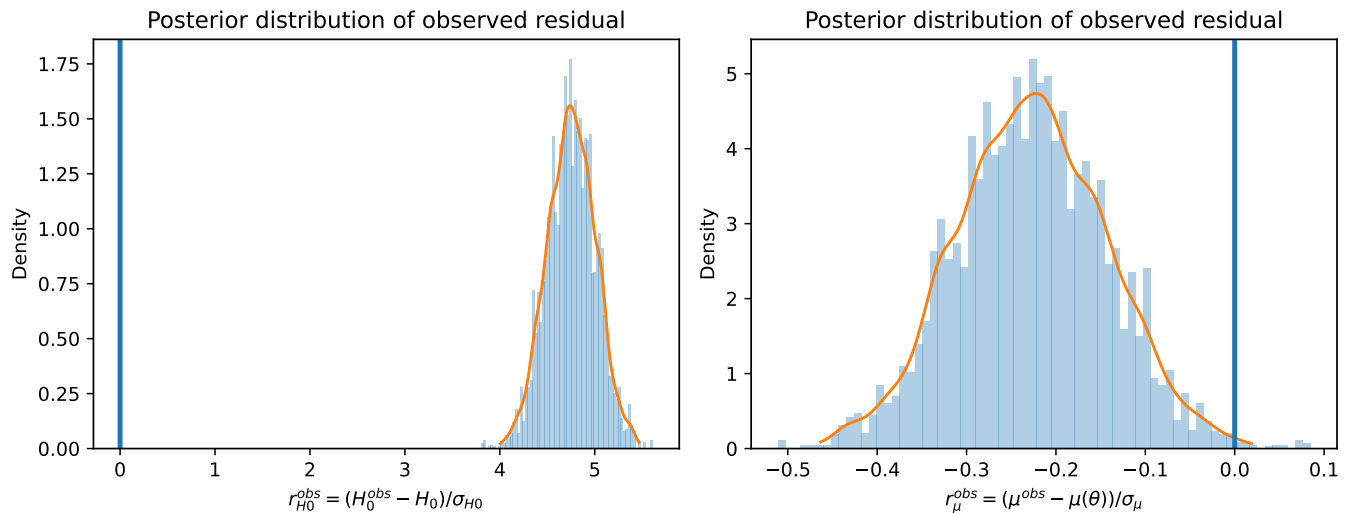


FIG. 3. Posterior predictive residual distributions for the Λ CDM model. Histograms show replicated discrepancies in H_0 and $\mu(z = 0.01)$ generated from posterior samples constrained by CMB and DESI DR2 data. The vertical line denotes the observed value in each case.

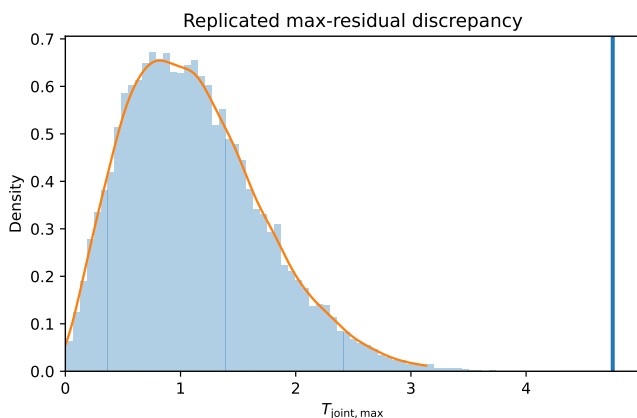


FIG. 4. Posterior predictive distribution of the maximum joint discrepancy statistic for Λ CDM. Replicated values are obtained from posterior draws, and the vertical line indicates the observed statistic.

the tail of the predictive distribution refer to Fig. 5, resulting in $p_{\text{ppc}}(H_0) \simeq 5 \times 10^{-5}$. This inconsistency is reinforced by the joint statistics, for which both the joint χ^2 and maximum discrepancy yield $p_{\text{ppc}} \simeq 5 \times 10^{-5}$. These results indicate that the observed combination of expansion-rate and distance information is highly atypical under Λ CDM. In contrast, the low-redshift supernova distance modulus is well reproduced, refer to Fig. 5, with $p_{\text{ppc}}(\mu) \simeq 0.81$, demonstrating that the tension does not originate from supernova distance calibration or luminosity systematics alone.

However, introducing the sign-switching cosmological constant in the Λ_s CDM model leads to a modest but systematic shift in the posterior predictive distributions toward higher values of H_0 . Quantitatively, this man-

ifests as an increase in the joint posterior predictive p -value to $p_{\text{ppc}}^{\text{joint}} \simeq 4 \times 10^{-4}$, indicating partial alleviation of the tension relative to Λ CDM. Nevertheless, the observed H_0 remains in the tail of the predictive distribution, and the joint discrepancy statistics continue to signal a statistically significant inconsistency. Importantly, the Λ_s CDM model preserves consistency with the low-redshift supernova distance observable, showing that the extension does not compromise the successful distance predictions of the standard model.

The corresponding PPC Figs. further illustrate this behavior. From Fig. 3, it is clear that the H_0 observed residual histogram is sitting around a large positive value, while the observed vertical line is far out in the tail. This means that Λ CDM predicts a lower value of H_0 than what is observed. Similarly, in Fig. 6, the observed residual H_0 still lies in the far tail, but the histogram peak appears slightly closer to what was observed for Λ CDM, indicating partial alleviation. Thus, Λ_s CDM shifts the late-time behavior enough to move predictions modestly toward the local H_0 , but the observed H_0 remains an outlier.

In Figs. 4 and 8, we can see that in both cases the observed vertical line is far to the right, showing that the data generate a discrepancy far larger than what Λ CDM typically predicts. However, for Λ_s CDM, the maximum discrepancy is less extreme than in Λ CDM. This is consistent with some improvement: Λ_s CDM reduces the most severe inconsistency but does not remove it.

Again, from the replicated distributions shown in Figs. 5 and 7 for the Λ CDM and Λ_s CDM models, it is clearly seen that H_0^{rep} is centred around a Planck-like value, with the observed value lying in the extreme right tail of the distribution. The replicated μ^{rep} distribution is tightly centered near the observed value, with the observed line

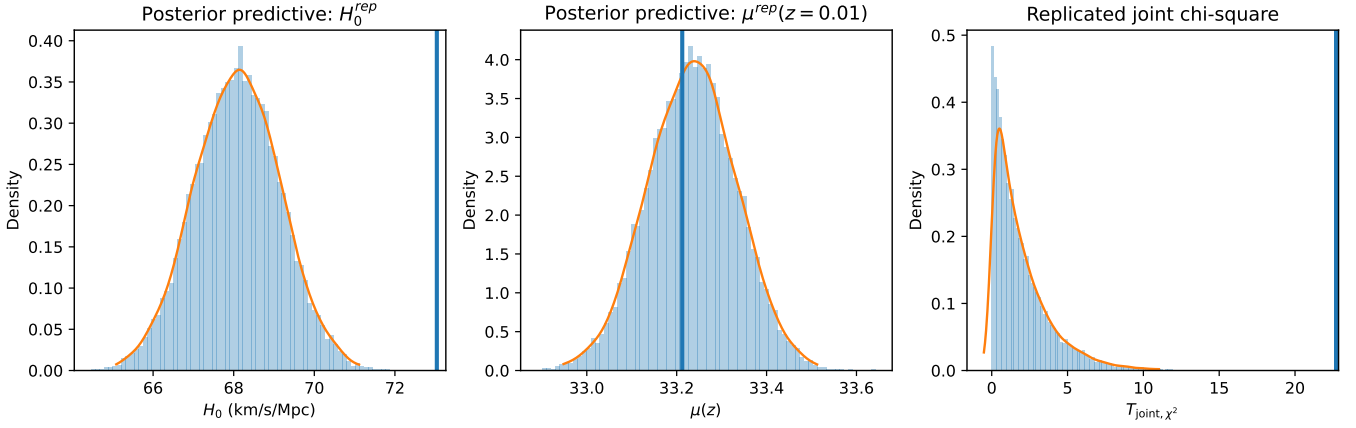


FIG. 5. Posterior predictive replicated distributions for Λ CDM showing H_0 , $\mu(z = 0.01)$, and the joint χ^2 statistic. Replicated values are generated from posterior samples; vertical lines mark the observed quantities.

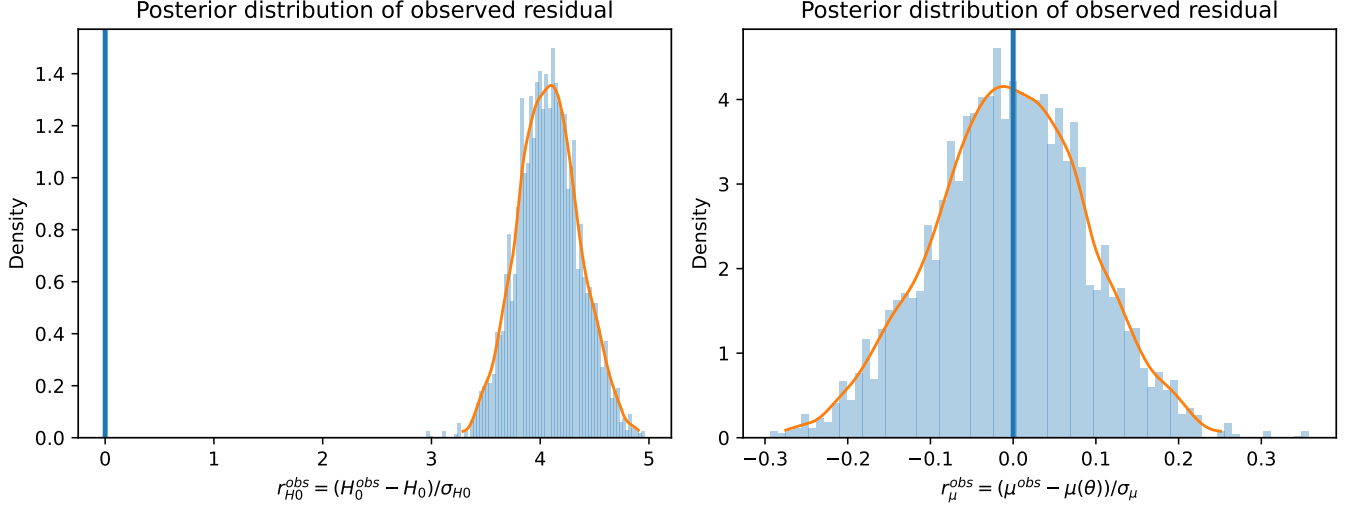


FIG. 6. Posterior predictive residual distributions for the Λ_s CDM model. Histograms show replicated discrepancies in H_0 and $\mu(z = 0.01)$ derived from posterior samples constrained by CMB and DESI DR2 data. Vertical lines denote the observed values.

lying well within the bulk. In addition, the replicated joint chi-squared distribution is heavily weighted toward low values, while the observed joint statistic lies far to the right, showing that the combined mismatch is very unlikely under Λ CDM. Similar behavior is seen in the Λ_s CDM replicated distributions; however, the joint chi-squared remains inconsistent, though the discrepancy is visually less stark than in Λ CDM. Thus, while the replicated distributions for μ encompass the observed value, the observed H_0 and joint discrepancy statistics consistently lie far outside the bulk of the posterior predictive distributions.

Overall, the PPC diagnostics demonstrate that while Λ_s CDM softens the Hubble tension compared to Λ CDM, it does not fully reconcile local expansion-rate measurements with CMB and large-scale-structure-anchored posteriors. The persistence of the inconsistency across multi-

ple discrepancy statistics and its stability against Monte Carlo uncertainty indicate that the residual tension reflects a genuine mismatch in late-time expansion dynamics rather than a statistical fluctuation or posterior-shape artifact. Thus, since Λ_s CDM does not effectively decouple the CMB and DESI DR2 ruler calibration in a way that permits a higher H_0 , it does not make SH0ES + calibrated low- z SN clearly consistent with the CMB+DESI-DR2 posterior, and these PPC results are consistent with the tension-metric analysis: Λ_s CDM reduces the severity of the late-time discrepancy relative to Λ CDM, but the observed H_0 (and joint discrepancy statistics) remain extreme under the posterior predictive distribution, while the low-redshift distance-modulus proxy is well reproduced.

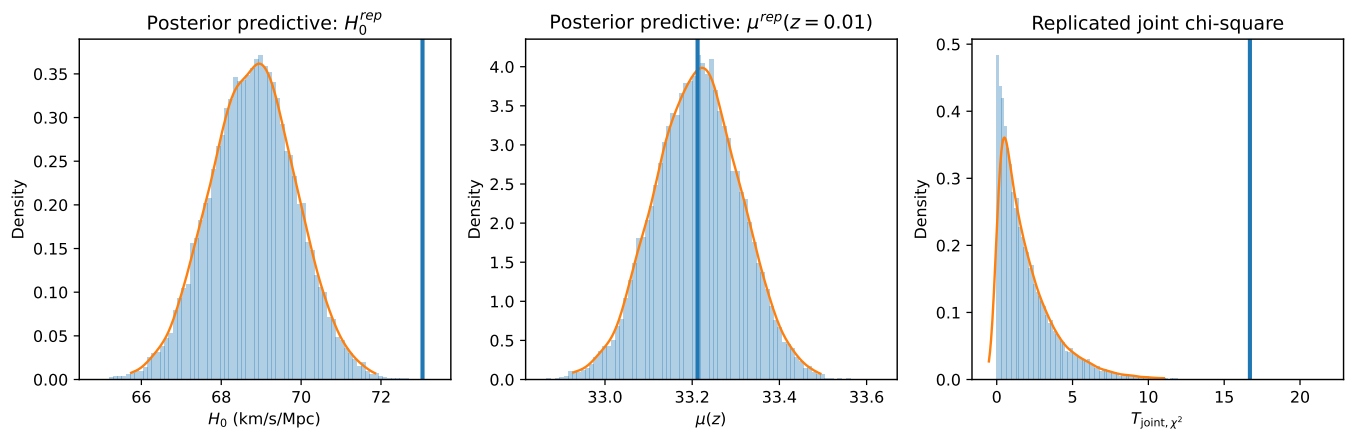


FIG. 7. Posterior predictive replicated distributions for Λ_s CDM showing H_0 , $\mu(z = 0.01)$, and the joint χ^2 statistic. Replicated samples are generated from the posterior; vertical lines indicate the observed values.

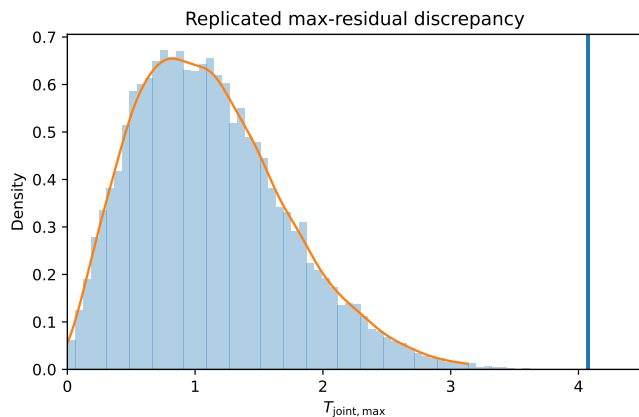


FIG. 8. Posterior predictive distribution of the maximum joint discrepancy statistic for Λ_s CDM. Replicated values are computed from posterior draws, with the observed statistic indicated by the vertical line.

VI. DISCUSSION

The statistical analyses presented in Sec. V show that apparent dataset inconsistency depends sensitively on the diagnostic employed, particularly when combining tightly constrained datasets with weakly informative and strongly non-Gaussian ones. In all configurations considered here, the combined CMB+DESI DR2 dataset yields a compact posterior that tightly constrains the shared parameter space, while the PPS dataset exhibits a substantially larger and highly non-Gaussian posterior. As a result, comparisons involving PPS are inherently asymmetric and require careful interpretation.

Gaussian tension metrics applied to Λ CDM indicate moderate disagreement between CMB and DESI DR2, and a much stronger discrepancy once PPS is included. When assessed using the exact non-Gaussian parameter-shift statistic, the CMB+DESI DR2 comparison shows

substantial posterior overlap, confirming excellent mutual consistency between early and intermediate-redshift probes. In contrast, comparisons involving PPS yield large exact parameter shifts, indicating statistically disjoint posterior support relative to the CMB+DESI DR2 constraints.

When PPS is updated with the highly constrained CMB+DESI DR2 posterior, this effect is more noticeable. Here, the accurate non-Gaussian parameter-shift statistic shows that the PPS posterior fills a specific region of parameter space, whereas updated Gaussian metrics enhance directional mean shifts caused by covariance compression. This shows that PPS-driven Gaussian tensions are not numerical variations of posterior geometry but rather reflect actual late-time inconsistencies, and thus Gaussian metrics alone cannot be used to reliably evaluate datasets with very large and non-Gaussian posteriors.

The Λ_s CDM model systematically reduces Gaussian and MAP-based tension measures across all dataset combinations. In particular, the CMB and DESI DR2 comparison exhibits tensions well below the 0.3σ level, indicating excellent mutual consistency once additional late-time flexibility is introduced. This improvement arises because Λ_s CDM allows expansion along degeneracy directions already present in the CMB data, thereby improving geometric compatibility without altering early-universe physics. In comparisons involving PPS, however, large Gaussian update tensions and significant exact non-Gaussian parameter shifts persist, confirming that the apparent inconsistency is driven by conflicting late-time parameter preferences rather than by posterior-shape effects alone. Relative to Λ CDM, Λ_s CDM shows smaller MAP displacements and reduced rule-of-thumb tensions, indicating a statistically improved but not fully consistent joint description of all datasets.

Concerning the posterior predictive consistency test, it provides an independent assessment of model adequacy that is insensitive to posterior geometry alone. For

Λ CDM, the observed local value of H_0 lies deep in the tail of the posterior predictive distribution derived from CMB+DESI DR2 data, yielding extremely small predictive p -values for both one-dimensional and joint discrepancy statistics. In contrast, the low-redshift distance-modulus proxy is well reproduced, indicating that the dominant tension originates from the late-time expansion rate rather than from supernova distance calibration.

In the Λ_s CDM case, the posterior predictive distributions shift modestly but systematically toward higher values of H_0 , leading to an increase in joint posterior predictive p -values and hence a partial alleviation of the discrepancy. However, the joint discrepancy statistics continue to show significant inconsistency, and the observed H_0 is still statistically unusual. Importantly, consistency with the low-redshift distance-modulus observable is preserved, demonstrating that the late-time modification does not compromise the successful distance predictions of the standard Λ CDM framework.

A key insight emerging from the posterior predictive analysis is the distinction between marginal and joint predictive adequacy. The Λ_s CDM modification alters the late-time background expansion in a way that preferentially affects one-dimensional observables such as H_0 , shifting the corresponding posterior predictive distribution toward higher values. However, this localized modification does not sufficiently reorganize the joint structure of expansion-rate and distance predictions required to render the combined (H_0, μ) discrepancy statistically typical. Consequently, improvements in marginal posterior predictive performance do not translate into full joint consistency. This explains why Λ_s CDM systematically softens but does not resolve the Hubble tension. Thus, the model modifies the late-time expansion history enough to shift H_0 , but not sufficiently to reconcile the global distance ladder implied by CMB and BAO calibrated posterior.

VII. CONCLUSION

In this work, we have explored the internal consistency of current cosmological datasets and the late-time predictive performance of the standard Λ CDM framework and its sign-switching extension, Λ_s CDM, by confronting them with a large combination of early, intermediate, and low-redshift observations. Our analysis combines Gaussian and non-Gaussian parameter space diagnostics with posterior predictive consistency tests to robustly evaluate cosmological tensions. It emphasizes that the interpretation of cosmological tensions depends sensitively on the statistical diagnostics employed, particularly when datasets with very different constraining power and posterior geometry are combined.

We find that Gaussian tension metrics can substantially overstate inconsistencies when datasets with very different constraining power and non-Gaussian posteriors are combined. We have shown that the exact non-

Gaussian parameter-shift statistics reveal excellent consistency between CMB and BAO datasets in both Λ CDM and Λ_s CDM models, with the Λ_s CDM model further improving geometric compatibility at intermediate redshifts. In contrast, comparisons involving PPS data yield large exact parameter shifts in both models, indicating disjoint posterior support to CMB and BAO constraints.

Our posterior predictive tests show that Λ CDM strongly disfavors the observed local value of the Hubble constant, while Λ_s CDM shifts late-time predictions toward higher H_0 values and partially alleviates the tension. Nevertheless, the observed expansion rate remains statistically atypical under the predictive distribution, and joint late-time discrepancies still persist. In summary, Λ_s CDM improves parameter space compatibility and softens several late-time tensions relative to Λ CDM, but does not fully reconcile local expansion-rate measurements with CMB and BAO calibrated posteriors. Hence, our results suggest the necessity of exact, non-Gaussian, and predictive diagnostics for reliably assessing cosmological model consistency, providing a robust benchmark for assessing future cosmological models and datasets. In a forthcoming work, we will extend this statistical framework to dynamical dark-energy parameterization via energy density [97] and other extended cosmological scenarios, to further assess their internal consistency and predictive performance across current cosmological datasets.

ACKNOWLEDGMENTS

S.K. (the first author) acknowledges the financial support and computational facilities provided by Plaksha University. A.J.S.C. acknowledges Conselho Nacional de Desenvolvimento Científico e Tecnológico (CNPq; National Council for Scientific and Technological Development) for partial financial support (Grant No. 305881/2022-1) and Fundação da Universidade Federal do Paraná (FUNPAR; Paraná Federal University Foundation) through public notice 04/2023-Pesquisa/PRPPG/UFPR for partial financial support (Process No. 23075.019406/2023-92), as well as the financial support of the NAPI “Fenômenos Extremos do Universo” of Fundação de Apoio à Ciência, Tecnologia e Inovação do Paraná (NAPI FÍSICA–FASE 2), under protocol No. 22.687.035-0. S.K. acknowledges the support of the Startup Research Grant from Plaksha University (File No. OOR/PU-SRG/2023-24/08). This article is based upon work from the COST Action CA21136 “Addressing observational tensions in cosmology with systematics and fundamental physics” (CosmoVerse), supported by COST (European Cooperation in Science and Technology).

- [1] D. H. Weinberg, M. J. Mortonson, D. J. Eisenstein, C. Hirata, A. G. Riess, and E. Rozo, *physrep* **530**, 87 (2013), arXiv:1201.2434 [astro-ph.CO].
- [2] D. N. Spergel *et al.* (WMAP), *Astrophys. J. Suppl.* **148**, 175 (2003), arXiv:astro-ph/0302209.
- [3] E. Komatsu, K. M. Smith, and o. Dunkley, *apjs* **192**, 18 (2011), arXiv:1001.4538 [astro-ph.CO].
- [4] N. Aghanim *et al.* (Planck), *Astron. Astrophys.* **641**, A6 (2020), [Erratum: *Astron. Astrophys.* 652, C4 (2021)], arXiv:1807.06209 [astro-ph.CO].
- [5] M. S. Madhavacheril *et al.*, *The Astrophysical Journal* **962**, 113 (2024).
- [6] W. J. Percival, S. Cole, *et al.*, *MNRAS* **381**, 1053 (2007).
- [7] F. Beutler and o. Blake, *mnras* **416**, 3017 (2011), arXiv:1106.3366 [astro-ph.CO].
- [8] D. Parkinson and o. Riemer-Sorensen, *prd* **86**, 103518 (2012), arXiv:1210.2130 [astro-ph.CO].
- [9] S. Alam *et al.* (eBOSS), *Phys. Rev. D* **103**, 083533 (2021), arXiv:2007.08991 [astro-ph.CO].
- [10] S. Alam, Ata, *et al.*, *MNRAS* **470**, 2617 (2017), arXiv:1607.03155 [astro-ph.CO].
- [11] A. G. Riess *et al.* (Supernova Search Team), *Astron. J.* **116**, 1009 (1998), arXiv:astro-ph/9805201.
- [12] S. Perlmutter *et al.* (Supernova Cosmology Project), *Astrophys. J.* **517**, 565 (1999), arXiv:astro-ph/9812133.
- [13] M. Bartelmann and P. Schneider, *Phys. Rept.* **340**, 291 (2001), arXiv:astro-ph/9912508.
- [14] X. Liu, C. Pan, and o. Li, *MNRAS* **450**, 2888 (2015), arXiv:1412.3683 [astro-ph.CO].
- [15] H. Shan, X. Liu, and o. Hildebrandt, *MNRAS* **474**, 1116 (2018), arXiv:1709.07651 [astro-ph.CO].
- [16] R. Mandelbaum, *ARAA* **56**, 393 (2018), arXiv:1710.03235 [astro-ph.CO].
- [17] C. Heymans *et al.*, *Astron. Astrophys.* **646**, A140 (2021), arXiv:2007.15632 [astro-ph.CO].
- [18] T. M. C. Abbott *et al.* (DES), *Phys. Rev. D* **105**, 023520 (2022), arXiv:2105.13549 [astro-ph.CO].
- [19] S. Weinberg, *Cosmology* (Oxford University Press, 2008).
- [20] P. J. Peebles and B. Ratra, *Reviews of Modern Physics* **75**, 559 (2003), arXiv:astro-ph/0207347 [astro-ph].
- [21] M. J. Mortonson, D. H. Weinberg, and M. White, arxiv-preprint (2013), arXiv:1401.0046 [astro-ph.CO].
- [22] D. Huterer and D. L. Shafer, *Rept. Prog. Phys.* **81**, 016901 (2018), arXiv:1709.01091 [astro-ph.CO].
- [23] D. Scolnic *et al.*, *Astrophys. J.* **938**, 113 (2022), arXiv:2112.03863 [astro-ph.CO].
- [24] A. G. Riess, W. Yuan, and o. Macri, *ApJL* **934**, L7 (2022), arXiv:2112.04510 [astro-ph.CO].
- [25] W. L. Freedman *et al.*, *Astrophys. J.* **882**, 34 (2019), arXiv:1907.05922 [astro-ph.CO].
- [26] W. L. Freedman, B. F. Madore, T. Hoyt, and others., *Astrophys. J.* **985**, 203 (2025), [Erratum: *Astrophys. J.* 993, 252 (2025)], arXiv:2408.06153 [astro-ph.CO].
- [27] S. Casertano *et al.* (H0DN), arXiv preprint (2025), arXiv:2510.23823 [astro-ph.CO].
- [28] L. Verde, T. Treu, and A. G. Riess, *Nature Astron.* **3**, 891 (2019), arXiv:1907.10625 [astro-ph.CO].
- [29] E. Abdalla *et al.*, *JHEAp* **34**, 49 (2022), arXiv:2203.06142 [astro-ph.CO].
- [30] E. Di Valentino *et al.* (CosmoVerse Network), *Phys. Dark Univ.* **49**, 101965 (2025), arXiv:2504.01669 [astro-ph.CO].
- [31] M. Kamionkowski and A. G. Riess, *Ann. Rev. Nucl. Part. Sci.* **73**, 153 (2023), arXiv:2211.04492 [astro-ph.CO].
- [32] M. Najafi, S. Pan, E. Di Valentino, and J. T. Firouzjaee, *Phys. Dark Univ.* **45**, 101539 (2024), arXiv:2407.14939 [astro-ph.CO].
- [33] Y. Akrami *et al.* (CANTATA), *Modified Gravity and Cosmology. An Update by the CANTATA Network* (Springer, 2021) arXiv:2105.12582 [gr-qc].
- [34] T. P. Sotiriou and V. Faraoni, *Rev. Mod. Phys.* **82**, 451 (2010), arXiv:0805.1726 [gr-qc].
- [35] E. Di Valentino, O. Mena, S. Pan, L. Visinelli, W. Yang, A. Melchiorri, D. F. Mota, A. G. Riess, and J. Silk, *Class. Quant. Grav.* **38**, 153001 (2021), arXiv:2103.01183 [astro-ph.CO].
- [36] Ö. Akarsu, J. D. Barrow, L. A. Escamilla, and J. A. Vazquez, *Phys. Rev. D* **101**, 063528 (2020), arXiv:1912.08751 [astro-ph.CO].
- [37] O. Akarsu, S. Kumar, E. Özülker, and J. A. Vazquez, *Phys. Rev. D* **104**, 123512 (2021), arXiv:2108.09239 [astro-ph.CO].
- [38] O. Akarsu, E. Di Valentino, S. Kumar, R. C. Nunes, J. A. Vazquez, and A. Yadav, arXiv preprint (2023), arXiv:2307.10899 [astro-ph.CO].
- [39] O. Akarsu, A. De Felice, E. Di Valentino, S. Kumar, R. C. Nunes, E. Ozulker, J. A. Vazquez, and A. Yadav, *Phys. Rev. D* **110**, 103527 (2024), arXiv:2406.07526 [astro-ph.CO].
- [40] M. Raveri and C. Doux, *Phys. Rev. D* **104**, 043504 (2021), arXiv:2105.03324 [astro-ph.CO].
- [41] M. Leizerovich, S. J. Landau, and C. G. Scoccola, *Phys. Lett. B* **855**, 138844 (2024), arXiv:2312.08542 [astro-ph.CO].
- [42] A. Gelman, X.-L. Meng, and H. Stern, *Statistica Sinica* **6**, 733 (1996).
- [43] C. Doux *et al.* (DES), *Mon. Not. Roy. Astron. Soc.* **503**, 2688 (2021), arXiv:2011.03410 [astro-ph.CO].
- [44] P. J. E. Peebles, *Principles of Physical Cosmology* (Princeton University Press, 2020).
- [45] B. Ryden, *Introduction to cosmology* (Cambridge University Press, 1970).
- [46] S. M. Carroll, *Spacetime and Geometry: An Introduction to General Relativity* (Cambridge University Press, 2019).
- [47] L. Amendola and S. Tsujikawa, *Dark Energy: Theory and Observations* (Cambridge University Press, 2015).
- [48] E. A. Paraskevas, A. Çam, L. Perivolaropoulos, and O. Akarsu, *Phys. Rev. D* **109**, 103522 (2024).
- [49] A. G. Riess *et al.*, *Astrophys. J. Lett.* **992**, L34 (2025), arXiv:2509.01667 [astro-ph.CO].
- [50] S. Birrer *et al.* (TDCOSMO), *Astron. Astrophys.* **704**, A63 (2025), arXiv:2506.03023 [astro-ph.CO].
- [51] R. Bousso and J. Polchinski, *JHEP* **06**, 006 (2000), arXiv:hep-th/0004134.
- [52] O. Akarsu, S. Kumar, E. Özülker, J. A. Vazquez, and A. Yadav, *Phys. Rev. D* **108**, 023513 (2023), arXiv:2211.05742 [astro-ph.CO].
- [53] A. Yadav, S. Kumar, C. Kibris, and O. Akarsu, *JCAP* **01**, 042 (2025), arXiv:2406.18496 [astro-ph.CO].
- [54] A. De Felice, A. Doll, and S. Mukohyama, *JCAP* **09**,

- 034 (2020), arXiv:2004.12549 [gr-qc].
- [55] B. Alexandre, S. Gielen, and J. Magueijo, *JCAP* **02**, 036 (2024), arXiv:2306.11502 [hep-th].
- [56] L. A. Anchordoqui, I. Antoniadis, and D. Lust, *Phys. Lett. B* **855**, 138775 (2024), arXiv:2312.12352 [hep-th].
- [57] L. A. Anchordoqui, I. Antoniadis, D. Bielli, A. Chatrabhuti, and H. Isono, *JHEP* **07**, 021 (2025), arXiv:2410.18649 [hep-th].
- [58] L. A. Anchordoqui, I. Antoniadis, D. Lust, N. T. Noble, and J. F. Soriano, *Phys. Dark Univ.* **46**, 101715 (2024), arXiv:2404.17334 [astro-ph.CO].
- [59] O. Akarsu, B. Bulduk, A. De Felice, *et al.*, *Phys. Rev. D* **112**, 083532 (2025), arXiv:2410.23068 [gr-qc].
- [60] M. S. Souza, A. M. Barcelos, R. C. Nunes, O. Akarsu, and S. Kumar, *Universe* **11**, 2 (2025), arXiv:2501.18031 [astro-ph.CO].
- [61] Ö. Akarsu, L. Perivolaropoulos, A. Tsikoundoura, A. E. Yükselci, and A. Zhuk, arXiv (2025), arXiv:2502.14667 [astro-ph.CO].
- [62] J. F. Soriano, S. Wohlberg, and L. A. Anchordoqui, *Phys. Dark Univ.* **48**, 101911 (2025), arXiv:2502.19239 [astro-ph.CO].
- [63] L. A. Escamilla, Ö. Akarsu, E. Di Valentino, E. Özüiker, and J. A. Vazquez, arXiv (2025), arXiv:2503.12945 [astro-ph.CO].
- [64] N. Aghanim *et al.* (Planck), *Astron. Astrophys.* **641**, A5 (2020), arXiv:1907.12875 [astro-ph.CO].
- [65] N. Aghanim *et al.* (Planck), *Astron. Astrophys.* **641**, A8 (2020), arXiv:1807.06210 [astro-ph.CO].
- [66] M. S. Madhavacheril *et al.* (ACT), *Astrophys. J.* **962**, 113 (2024), arXiv:2304.05203 [astro-ph.CO].
- [67] T. Louis *et al.* (Atacama Cosmology Telescope), *JCAP* **11**, 062 (2025), arXiv:2503.14452 [astro-ph.CO].
- [68] Z. Pan *et al.* (SPT), *Phys. Rev. D* **108**, 122005 (2023), arXiv:2308.11608 [astro-ph.CO].
- [69] D. Dutcher *et al.* (SPT-3G), *Phys. Rev. D* **104**, 022003 (2021), arXiv:2101.01684 [astro-ph.CO].
- [70] L. Balkenhol *et al.* (SPT-3G), *Phys. Rev. D* **108**, 023510 (2023), arXiv:2212.05642 [astro-ph.CO].
- [71] S. M. Feeney, D. J. Mortlock, and N. Dalmaso, *Mon. Not. Roy. Astron. Soc.* **476**, 3861 (2018), arXiv:1707.00007 [astro-ph.CO].
- [72] J. Lesgourgues, arXiv e-prints, arXiv:1104.2932 (2011), arXiv:1104.2932 [astro-ph.IM].
- [73] C.-P. Ma and E. Bertschinger, *Astrophys. J.* **455**, 7 (1995), arXiv:astro-ph/9506072.
- [74] M. Bouhmadi-Lopez and B. Ibarra-Uriondo, *Phys. Dark Univ.* **50**, 102129 (2025), arXiv:2506.18992 [gr-qc].
- [75] V. Mukhanov, H. Feldman, and R. Brandenberger, *phys-rep* **215**, 203 (1992).
- [76] M. Leizerovich, S. J. Landau, and C. G. Scóccola, *Phys. Lett. B* **855**, 138844 (2024), arXiv:2312.08542 [astro-ph.CO].
- [77] C. P. Robert, arXiv e-prints, arXiv:1504.01896 (2015), arXiv:1504.01896 [stat.CO].
- [78] A. Gelman and D. B. Rubin, *Statistical Science* **7**, 457 (1992).
- [79] D. Vats and C. Knudson, arXiv e-prints, arXiv:1812.09384 (2018), arXiv:1812.09384 [stat.CO].
- [80] R. G. Staudte, arXiv e-prints, arXiv:1912.01134 (2019), arXiv:1912.01134 [math.ST].
- [81] M. Raveri and W. Hu, *Phys. Rev. D* **99**, 043506 (2019), arXiv:1806.04649 [astro-ph.CO].
- [82] P. Lemos *et al.* (DES), *Mon. Not. Roy. Astron. Soc.* **505**, 6179 (2021), arXiv:2012.09554 [astro-ph.CO].
- [83] L. Verde, T. Treu, and A. G. Riess, *Nature Astronomy* **3**, 891 (2019), arXiv:1907.10625 [astro-ph.CO].
- [84] W. L. Freedman, *Astrophys. J.* **919**, 16 (2021), arXiv:2106.15656 [astro-ph.CO].
- [85] P. Lemos *et al.* (DES), *Mon. Not. Roy. Astron. Soc.* **505**, 6179 (2021), arXiv:2012.09554 [astro-ph.CO].
- [86] W. Handley and P. Lemos, *Phys. Rev. D* **100**, 043504 (2019).
- [87] M. Raveri, G. Zacharegkas, and W. Hu, *Phys. Rev. D* **101**, 103527 (2020), arXiv:1912.04880 [astro-ph.CO].
- [88] D. J. Spiegelhalter, N. G. Best, B. P. Carlin, and A. van der Linde, *J. Roy. Statist. Soc. B* **64**, 583 (2002).
- [89] P. C. Mahalanobis, *J. Proc. Asiatic Soc. Bengal* **23**, 301 (1927).
- [90] P. Mahalanobis, *Proc. Natl. Inst. Sci. India* **12**, 49 (1936).
- [91] R. De Maesschalck, D. Jouan-Rimbaud, and D. Massart, *Chemometr. Intell. Lab. Syst.* **50**, 1 (2000).
- [92] S. M. Lynch, in *Encyclopedia of Social Measurement*, edited by K. Kempf-Leonard (Elsevier, New York, 2005) pp. 135–144.
- [93] H. Sennhenn-Reulen, arXiv e-prints, arXiv:2412.15809 (2024), arXiv:2412.15809 [stat.ME].
- [94] X.-L. Meng, *The Annals of Statistics* **22**, 1142 (1994).
- [95] H. Sennhenn-Reulen, arXiv e-prints, arXiv:2412.15809 (2024), arXiv:2412.15809 [stat.ME].
- [96] A. G. Riess *et al.*, *Astrophys. J. Lett.* **934**, L7 (2022), arXiv:2112.04510 [astro-ph.CO].
- [97] S. Kumar, *Phys. Dark Univ.* **52**, 102248 (2026), arXiv:2512.19000 [astro-ph.CO].